



HAL
open science

Numerical Modeling of Acousto–Plasmonic Coupling in Metallic Nanoparticles

Ophélie Saison-Francioso, Gaëtan Lévêque, Abdellatif Akjouj

► **To cite this version:**

Ophélie Saison-Francioso, Gaëtan Lévêque, Abdellatif Akjouj. Numerical Modeling of Acousto–Plasmonic Coupling in Metallic Nanoparticles. *Journal of Physical Chemistry C*, 2020, 124 (22), pp.12120-12133. 10.1021/acs.jpcc.0c00874 . hal-02939402

HAL Id: hal-02939402

<https://hal.science/hal-02939402v1>

Submitted on 15 Sep 2020

HAL is a multi-disciplinary open access archive for the deposit and dissemination of scientific research documents, whether they are published or not. The documents may come from teaching and research institutions in France or abroad, or from public or private research centers.

L'archive ouverte pluridisciplinaire **HAL**, est destinée au dépôt et à la diffusion de documents scientifiques de niveau recherche, publiés ou non, émanant des établissements d'enseignement et de recherche français ou étrangers, des laboratoires publics ou privés.

Numerical Modeling of Acousto-Plasmonic Coupling in Metallic Nanoparticles

Ophélie Saison-Francioso*, Gaëtan Lévêque, and Abdellatif Akjouj

Institut d'Électronique, de Microélectronique et de Nanotechnologie, CNRS UMR 8520, Département de Physique, FST, Université de Lille, 59655 Villeneuve d'Ascq, France

*Corresponding author: ophelie.saison-francioso@univ-lille.fr

ABSTRACT:

We describe a computational approach to study the acousto-plasmonic coupling in metallic nanoparticles. We use the high level multiphysics finite element software FreeFEM developed at Laboratoire Jacques-Louis Lions of Pierre and Marie Curie University (Paris). Our numerical method determines one after the other the acoustic modes of the nanoparticles and the modulation of the electromagnetic properties. The transfer of the deformed geometries between acoustic and electromagnetic simulations is realized by an update of the nodal coordinates situated at the boundary between the nanoparticle and its host medium, and using a mesh deformation algorithm based on radial basis function interpolation. Thus we theoretically investigate different coupling mechanisms between confined vibrations and surface plasmons: shape effect, electron density effect due to changes of the nanoparticle volume and inter-band transitions effect which is evaluated by the deformation potential mechanism.

1 INTRODUCTION

Nanoparticle research is a very active area in condensed matter physics. Potential applications concern various fields like chemistry¹, medicine², quantum information³, photonics.^{4,5} The optical properties of noble metal nanoparticles are dominated by the coupling between incident electromagnetic radiations and collective oscillations of conduction electrons. Resulting localized surface plasmon resonances have attracted a significant interest especially for the development of label-free sensor platforms.⁶⁻⁹ Due to mechanical confinement, noble metal nanoparticles also exhibit discrete vibrational modes. The vibrational properties are intensively explored by optical techniques taking advantage of plasmonic coupling such as Raman spectroscopy^{10,11} or time-resolved pump-probe experiments¹². The acoustic signature is related to the surrounding environment and is envisaged to be used to design nanobalances¹³. Both acoustic¹⁴⁻¹⁶ and optical¹⁷⁻¹⁹ characteristics are sensitive to many parameters such as the size, the shape, the coupling between the nanoparticles and the surrounding medium. Exploring the interaction between acoustic vibrations and localized surface plasmons have large fundamental and technological interests.²⁰⁻²³ For example, we can cite the development of multifunctional nanoagents integrating both tumor diagnosis and treatment functions.²⁴ Numerical modeling, by making possible the comparison of many different options for optimization, is an essential tool in the field of engineering novel nanostructures with high performances.^{25,26}

In this paper, the theoretical investigation and understanding of the acousto-plasmonic coupling have been performed by using Finite Element Method (FEM) calculations. Recently, Ahmed et al²⁷ numerically studied how acoustic vibrations modulate the optical response of plasmonic nanoparticles. Their method allows to quantitatively determine the coupling between a plasmon mode and a phonon mode, whatever the nanoparticle geometry. Furthermore, it is possible to separately evaluate the contribution of different coupling mechanisms. Confined vibrations modify the plasmonic response by way of surface and volume mechanisms.²⁸ Optomechanical coupling refers to surface coupling mechanism which involves changes of the particle shape associated with a modulation of the surface charges distribution. Photoelastic coupling is related to volume coupling mechanisms which imply changes of the metal dielectric permittivity. Two kinds of contributions can take place. Firstly, variations of the nanoparticle volume lead to modifications of the free electrons density. Secondly, strains of the metallic lattice due to acoustic phonons induce shifts in the band-structure. This phenomenon known as deformation potential mechanism has been theoretically developed by Bardeen and Shockley.²⁹

In order to study the acousto-plasmonic coupling in gold nanoparticles, we made the choice to use open-source softwares. We especially work with the high level multiphysics finite element software FreeFEM developed at Laboratoire Jacques-Louis Lions of Pierre and Marie Curie University (Paris). We implemented the modulation of the gold dielectric permittivity induced by acoustic vibrations described by Ahmed et al.²⁷ To take into account surface coupling mechanism, FreeFem simply allows to deform the nanoparticle after acoustic calculations. The transfer of the deformed geometries between acoustic and electromagnetic simulations is realized by an update of the nodal coordinates situated at the boundary between the nanoparticle and its host medium. We added a mesh deformation algorithm based on radial basis function interpolation³⁰ to adapt meshes whatever the shape modifications. Radial basis function interpolation is particularly used for fluid-structure interaction computations. We can cite for example the analysis of the bridges stability subjected to wind loads. Here, we apply this method to nanosystems in order to adapt the computational grid to the MNP deformations caused by acoustic vibration modes. Thus, it is possible to automate the launch of acousto-plasmonic coupling simulations for different acoustic modes and deformation amplitudes of interest. Our computational approach is different from Ahmed et al²⁷ one which is based on the use of three different softwares: the finite element solver COMSOL Multiphysics to perform acoustic calculations, Lumerical FDTD Solutions for optical calculations and MATLAB to transfer the deformed geometries. Our approach seems easier to use since we only need FreeFem to determine one after the other the acoustic modes of the nanoparticles and the modulation of the optical properties. Moreover, we doesn't have to transfer acoustic data obtained from a tetrahedral mesh of the nanostructure to a cuboid mesh in order to perform electromagnetic simulations by FDTD method.

This paper firstly describes the theoretical background required to study the acousto-plasmonic coupling. There are three major stages: 1) Characterization of the acoustic vibration modes and mechanical deformation of the nanoparticle, 2) Modulation of the metal dielectric permittivity under the influence of elastic strains, 3) Optical properties calculation. Secondly, we detail our methodology for numerical simulations and we briefly present the open-source softwares chosen to perform calculations. Thirdly, we discuss the results obtained for gold nanoparticles with different shapes: a sphere, a rod and a triangular prism with rounded edges and corners.

2 METHOD

2.1 Modelling acoustic and optical properties

The study of the acousto-plasmonic coupling combines two branches of physics. Mechanics

of continuous media allows to describe the deformations (strains) in the object of interest and electromagnetism is used to characterize the plasmonic response. In this paper, we consider the vibrational properties of free single metallic nanoparticles (MNP). Thus, we neglected mechanical interactions with the surrounding environment which shift the frequencies and damp oscillations³¹. Eigenmodes are determined by linear elasticity theory calculations^{32,33} and using bulk elastic constants of the materials (density, elastic coefficients). This approach generally agrees well with experimental measurements.^{34,35} The relation between strains and displacements is described by the Cauchy's strain tensor as we consider infinitesimal deformations. And the relation between strains and stresses is described by Hooke's law, which for linear-elastic and isotropic materials, only depends on the two Lamé constants (λ , μ). The nanoparticle eigenmodes correspond to harmonic solutions of Navier equation¹⁰:

$$-\rho \omega^2 \vec{u} = (\lambda + 2\mu) \vec{\nabla} (\vec{\nabla} \cdot \vec{u}) - \mu \vec{\nabla} \wedge (\vec{\nabla} \wedge \vec{u}) \quad (1)$$

where \vec{u} is the displacement field which we want to calculate, ρ is the density of the metal constituting the nanoparticle and ω is the eigenmode frequency. For the optical properties study, we consider the plane wave illumination of a single metallic nanoparticle embedded in a homogeneous dielectric medium. We solve the vector wave equation for the time-harmonic scattered electric field, the total field being the sum of the incoming field and the scattered field from the nanoparticle³⁶:

$$\vec{\nabla} \wedge \vec{\nabla} \wedge \vec{E}_{sca} - \varepsilon(\vec{r}) k_0^2 \vec{E}_{sca} = (\varepsilon(\vec{r}) - \varepsilon_b) k_0^2 \vec{E}_{inc} \quad (2)$$

where \vec{E}_{inc} is the incident field, \vec{E}_{sca} is the scattered field, k_0 is the free-space wavenumber, ε_b is the real-valued relative permittivity of the dielectric background.

2.2 Relation between metal dielectric permittivity and elastic strains

Some acoustic vibration eigenmodes can produce local volume changes which modulate the nanoparticle dielectric permittivity. To describe the MNP optical properties, we use a Lorentz-Drude model:

$$\varepsilon_r(\omega) = \varepsilon_r(\infty) + \omega_p^2 \sum_{m=0}^2 \frac{f_m}{\omega_{0,m}^2 - \omega^2 - j\omega \Gamma_m} \quad (3)$$

where $\varepsilon_r(\infty)$ is the dielectric constant at infinite frequency, ω_p is the bulk plasma frequency, f_m is the strength of the m^{th} Lorentzian damped harmonic oscillator, $\omega_{0,1}$ and $\omega_{0,2}$ correspond to inter-band transition frequencies ($\omega_{0,0}=0$) and Γ_m are damping frequencies. **Table 1** gathers the

parameters values used for calculations which are those of reference 27. Acoustic vibrations modulate both the Drude part and the Lorentz part of the relative permittivity.

Concerning the Drude part, the compression/expansion mechanisms inside the nanoparticle produce an increase/decrease of the free electron density. This affects the bulk plasma frequency which is equal to:

$$\omega_p = \sqrt{\frac{Ne^2}{\epsilon_0 m_e}} \quad (4)$$

where N is the local free electron density of the deformed nanoparticle, e is the electron charge, ϵ_0 is the free space permittivity and m_e is the effective mass of electron. The free electron density N depends on local dilation (dV/V) which, provided small deformations, can be evaluated using the trace of the strain tensor $\bar{\epsilon}$:

$$N = \frac{N_0}{1+dV/V} \quad (5)$$

$$\frac{dV}{V} = e_{xx} + e_{yy} + e_{zz} \quad (6)$$

where N_0 is the free electron density of the non-deformed nanoparticle and e_{xx}, e_{yy}, e_{zz} are the diagonal elements of $\bar{\epsilon}$. The strain tensor trace is given by acoustic calculations since it is equal to the displacement field divergence.

The Lorentz part of the permittivity is modulated because acoustic vibrations induce metallic lattice strains which shift the electronic band-structure. As a consequence, the inter-band transition frequencies are modified. Changes of inter-band transition frequencies due to local compression/dilatation phenomenon in the MNP are evaluated using deformation potentials³⁷:

$$\delta E_{0,m} = \xi_m \frac{dV}{V} \quad (7)$$

$$\omega'_{0,m} = \omega_{0,m} + \frac{\delta E_{0,m} |e|}{\hbar} \quad (8)$$

where $\delta E_{0,m}$ is the energy change associated with the m^{th} inter-band transition (eV), ξ_m are the deformation potentials, dV/V is the local dilatation, $|e|$ is the absolute value of the electron charge and \hbar is the reduced Planck's constant.

$\varepsilon_r(\infty)$	ω_p	$\omega_{0,1}$	$\omega_{0,2}$	Γ_0	Γ_1	Γ_2	f_0	f_1	f_2	ξ_1	ξ_2
	(10^{15} rad/s)									(eV)	
5.5	13.716	4.428	5.746	0.05979	1.070	1.690	1.039	0.1108	0.3202	-0.8	-9.0

Table 1: Values of the parameters used to model the gold relative dielectric permittivity with and without acousto-plasmonic coupling²⁷.

2.3 Step by step procedure for solving acousto-plasmonic coupling problems

We employ FEM³⁸ to approximate the solutions of the partial differential equations (PDE) describing the physical properties of interest. FEM is a variational method and first of all, the problem needs to be converted from its strong formulation to an alternative integral version called weak formulation. Basically, the PDE is multiplied by an arbitrary function $\vec{v}(x, y, z)$ named *test function* which belongs to the finite dimensional vector space Vh where the approximate solution is searched. The resulting expression is then integrated all over the domain. Finally, the highest derivative order is reduced by an integration by parts which makes appear the boundary conditions. The weak formulations of our problem with free boundary condition for the acoustic part and with a spherical Perfectly Matched Layer (PML)³⁹ for the optical part are respectively:

$$\iiint_{\Omega_{NP}} \left(-\omega^2 \rho \vec{v} \cdot \vec{u} + 2 \mu \bar{\varepsilon} : \text{grad}(\vec{v}) + \lambda \text{div}(\vec{u}) \text{div}(\vec{v}) \right) d\Omega_{NP} = 0 \quad (9)$$

$$\iiint_{\Omega} \left[\left(\vec{\nabla} \wedge \vec{E}_{sc} \right) \cdot \left(\nabla \wedge \vec{v} \right) \Lambda^{-1} - \varepsilon(\vec{r}) k_0^2 \Lambda \vec{E}_{sc} \cdot \vec{v} \right] d\Omega = \iiint_{\Omega_{NP}} \left(\varepsilon_{NP} - \varepsilon_b \right) k_0^2 \vec{E}_{inc} \cdot \vec{v} d\Omega_{NP} \quad (10)$$

where $\bar{\varepsilon}$ is the strain tensor and ε_{NP} is the frequency dependent complex-valued relative permittivity of the nanoparticle. The symbol Ω_{NP} represents the volume occupied by the nanoparticle. The symbol Ω represents the whole domain: the MNP, the dielectric background and the PML. The coefficient Λ is equal to 1 outside the PML and is a complex number inside the PML in order to avoid reflections at the edge of the computational domain.

The finite dimensional approximation space Vh is defined by the decomposition of the computational domain into small elements and the choice of a set of basis functions which linear combination gives a good approximation of the solution over a local element. Inserting the finite element approximation into the weak formulation transforms the problem from solving an integral equation to solving a system of linear equations. Each finite element is associated to a system of linear equations or a matrix equation. The components of the local element matrices are assembled to a global matrix in order to build the global system of equations for the whole domain. The basis

functions having a compact support (they are nonzero only on a small portion of the domain), the global matrix is very sparse and the equation system can be efficiently solved by a computer.^{40,41} We use the linear algebra solver MUMPS (**M**U**l**tifrontal **M**assively **P**arallel sparse direct **S**olver). It solves systems of linear equations via a direct method based on matrix factorization⁴² and contributes to reduce computation time as it is a parallel solver.

Figure 1 describes the main steps realized during the finite element analysis of the acousto-plasmonic coupling (see Supporting Information for validation results of the numerical method). We use Gmsh, an open-source 3-D finite element grid generator⁴³ to create geometries and unstructured tetrahedral meshes of the systems studied. Gmsh allows to define groups of elementary geometric entities in order to divide the computational domain into different volumes corresponding to the different materials (MNP, host matrix, PML). In this way, it is possible to assign them the parameters that describe their physical properties. Physical surfaces of interest are also designated like the nanoparticle surface, or planes of symmetry which are useful to reduce runtime and memory cost. It allows to apply appropriate boundary conditions or to process acoustic data required for optical calculations. Indeed, optical calculations are performed using the mesh of the MNP, its host matrix and the PML which absorb waves traveling outward the computational domain. As for acoustic calculations, they are only performed on the MNP mesh in order to determine its free vibration eigenmodes. Thus, the points displacements at the nanoparticle surface are needed to transfer the deformed geometries between acoustic and optical simulations. Finite element calculations are realized with the help of the free software FreeFEM⁴⁴. It requires to write scripts in its own language whose syntax is close to C++. For acoustic calculations, we work with a node-based finite element method⁴⁰ and use tetrahedral Lagrange P2 elements which possess 10 nodes situated at each vertex and at the middle of the edges. Thus, the displacement fields coordinates associated to vibration eigenmodes are approximated in the form of quadratic polynomials. To calculate the vibration eigenmodes of the MNP, its mesh is extracted from the mesh created by Gmsh. For that, we wrote a FreeFEM script which looks for the mesh data associated to the MNP and uses them to create a new mesh file. After acoustic calculations, we obtain several vibration eigenmodes. FreeFEM have a specific command to deform the nanoparticle from the displacement field. The deformation amplitude can be modified with ease and consequently, we can choose to perform optical calculations for different eigenmodes and deformations. Before each optical calculation, a new mesh file has to be created in order to transfer the deformed MNP into its host matrix. We use the displacement field obtained after acoustic calculations to update the nodal coordinates situated at MNP surface. We also implemented a mesh deformation algorithm based on radial basis function interpolation to insure that elements don't overlap or penetrate each other at the boundary between the nanoparticle and its host matrix. It is also a way to preserve shape regularity

of finite elements which determines meshes quality. The transfer of the deformed geometries is much detailed in the next section. To estimate the effect of vibration eigenmodes on the metal permittivity, we need local strains at the surface and inside the MNP given by acoustic calculations. As FreeFEM allows automatic interpolation of data from a mesh to another one, it is easy to transfer acoustic data needed. Optical calculations are performed using an edge-based finite element method introduced by Nédélec⁴⁵. The basis functions are not scalar any more but vectorial in order to be appropriate to approximate electric fields³⁹. Indeed, they fit the physical continuity properties of the electric field across inter-element interfaces (continuous tangential components and discontinuous normal components). In our simulations, we use second-order Nédélec tetrahedral finite elements to approximate the scattered electric field. Finally, the numerical results can be exported in the vtk format⁴⁶ or in text files in order to post-process data using respectively Paraview⁴⁷ (a data analysis and visualization application) or Gnuplot (a command-line driven graphing utility).

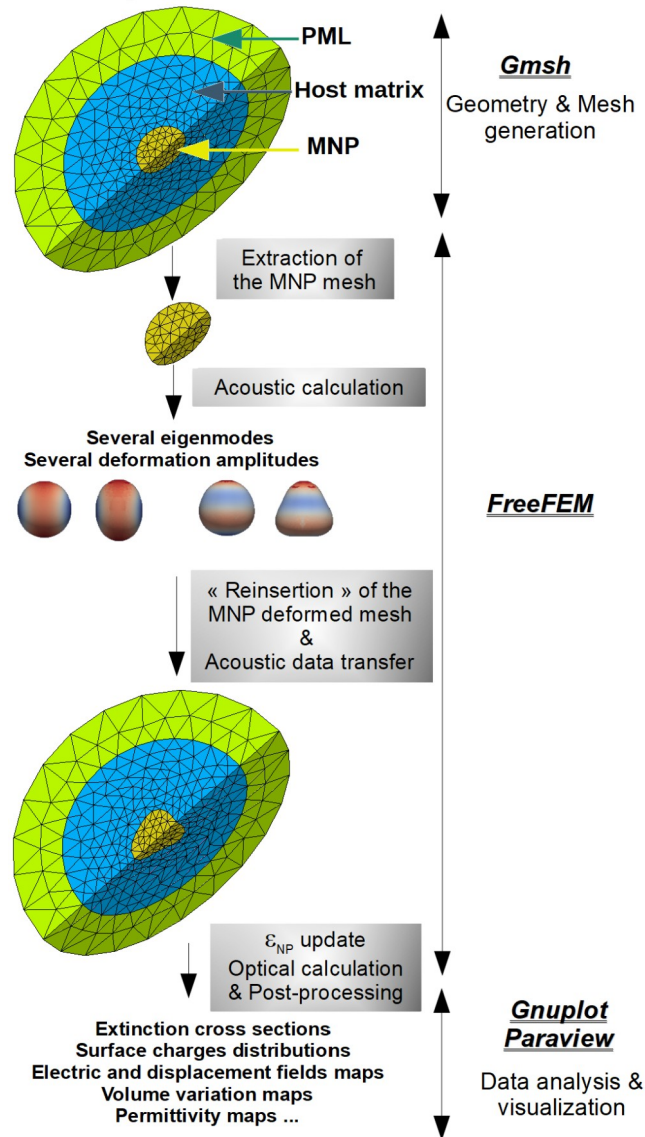


Figure 1: Schematic representation of the main steps of the acousto-plasmonic coupling study.

2.4 Transfer of the deformed geometries between acoustic and optical calculations

Acoustic simulations give several eigenmodes of vibration which deform the MNP. The transfer of the deformed geometries in the mesh of the dielectric host matrix surrounded by PML allows to study the portion of the acousto-plasmonic coupling due to shape effects. After acoustic simulations, new meshes of the free MNP are created from the calculated displacement fields. Those meshes correspond to different vibration eigenmodes and different deformation amplitudes. Our algorithm looks for all the points belonging to the triangles forming the mesh of the undeformed MNP surface in the Gmsh file and updates their coordinates according to the deformed MNP mesh files. The other nodal coordinates are remaining those given by Gmsh.

In order to be able to treat a large variety of nanoparticles, vibration eigenmodes and deformation amplitudes, we also implemented a mesh deformation algorithm based on radial basis function interpolation³⁰ (RBFi). It allows to preserve the shape regularity of finite elements at the boundary MNP/host matrix and prevents overlapping of finite elements. **Figure 2** illustrates the effect of the mesh deformation algorithm for an unrealistic extension of a gold nanorod. Updating the nodal coordinates associated to the MNP surface produces a finite element stretching on the side of the MNP while the finite elements on the side of the host matrix tend to collapse. Moreover, if the deformation is important compared to the mesh size, finite elements can overlap (**Fig. 2a**). RBFi overcomes those mesh issues by allowing to realize a smoothly point-by-point mesh movement around the interface MNP/host matrix (**Figs. 2b** and **c**). Thus, RBFi method is an easy way to study acoustic vibrations of complex-shaped metallic nanoparticles. Moreover, the method is highly efficient even for large deformations.

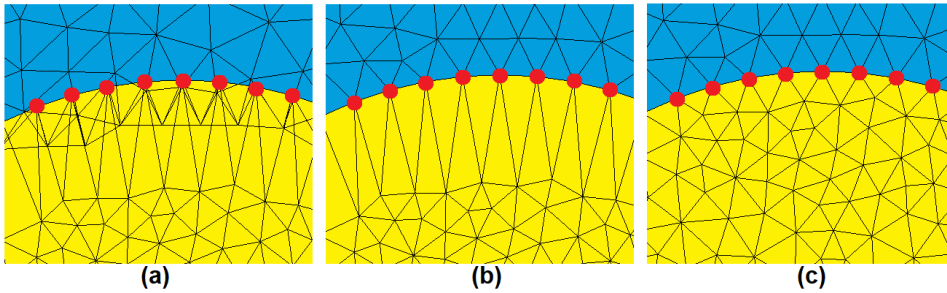


Figure 2: Illustration of the effect of RBFi. Blue triangles correspond to the host matrix, yellow triangles to the MNP and red dots to the nodes which coordinates are updated from the new MNP mesh files given by acoustic simulations. **(a)** Update of the nodal coordinates at the MNP surface only. **(b)** RBFi applied on host matrix side. **(c)** RBFi applied on both sides of the boundary MNP/host matrix.

In practice, the method involves determining a displacement function $d(\vec{r})$ to interpolate the nodes displacements around the interface MNP/host matrix:

$$d(\vec{r}) = \sum_{j=1}^{n_b} \alpha_j \varphi(\|\vec{r} - \vec{r}_{b_j}\|) + \sum_{k=1}^4 \beta_k \Pi_k(\vec{r}) \quad (11)$$

where n_b is the number of points belonging to the MNP surface, $\varphi(\|\vec{r} - \vec{r}_{b_j}\|)$ is the radial basis function, $\|\vec{r} - \vec{r}_{b_j}\|$ is the distance between the position vector \vec{r} of a node situated around the interface MNP/host matrix and the position vector \vec{r}_{b_j} of a node belonging to the MNP surface, $\Pi_k(\vec{r})$ corresponds to the basis of the space of linear trivariate polynomials $\{\Pi_1, \Pi_2, \Pi_3, \Pi_4\} = \{1, x, y, z\}$, α_j and β_k are weighted coefficients. There are many types of radial basis functions^{48,49} and we work with Wendland's C^2 which are commonly selected to perform mesh deformation⁵⁰:

$$\varphi(\xi) = (1 + 4\xi)(1 - \xi)_+^4 \quad (12)$$

They have a compact support which means only the internal mesh points inside a sphere with a radius s_r around a center situated at \vec{r}_{b_j} are influenced by the movement of the MNP surface points:

$$(1 - \xi)_+^4 = \begin{cases} (1 - \xi)^4 & \text{if } 0 \leq \xi < 1 \\ 0 & \text{if } \xi \geq 1 \end{cases} \quad (13)$$

where $\xi = \|\vec{r} - \vec{r}_{b_j}\|/s_r$, s_r being the support radius.

The displacement function is known for all the points belonging to the MNP surface from acoustic calculations. The nodal displacements around the MNP surface can be interpolated separately for each spatial direction. Thus, it is possible to build three systems of linear equations in order to determine the weighted coefficients.

$$\begin{bmatrix} d_b \\ 0 \end{bmatrix} = \begin{bmatrix} M_b & P_b \\ P_b^T & 0 \end{bmatrix} \begin{bmatrix} \alpha \\ \beta \end{bmatrix} \quad (14)$$

For (Ox) direction, we have the following boundary nodes displacements:

$$\begin{bmatrix} d_b \\ 0 \end{bmatrix} = \begin{bmatrix} \Delta x_1 \\ \Delta x_2 \\ \cdot \\ \cdot \\ \cdot \\ \Delta x_{n_b} \\ 0 \\ 0 \\ 0 \\ 0 \end{bmatrix}, \Delta x_i = x_{i,f} - x_{i,in} \quad (15)$$

where $x_{i,f}$ refer to the final nodal coordinates (MNP deformed by acoustic vibrations) and $x_{i,in}$ refer to the initial nodal coordinates (undeformed MNP). P_b is a $n_b \times 4$ matrix which contains the coordinates of the nodes situated at the surface of the undeformed MNP:

$$P_b = \begin{bmatrix} 1 & x_{1,\text{in}} & y_{1,\text{in}} & z_{1,\text{in}} \\ 1 & x_{2,\text{in}} & y_{2,\text{in}} & z_{2,\text{in}} \\ \cdot & \cdot & \cdot & \cdot \\ \cdot & \cdot & \cdot & \cdot \\ \cdot & \cdot & \cdot & \cdot \\ 1 & x_{n_b,\text{in}} & y_{n_b,\text{in}} & z_{n_b,\text{in}} \end{bmatrix} \quad (16)$$

M_b is a $n_b \times n_b$ matrix which contains radial basis functions for all the points belonging to the MNP surface and can be seen as a connectivity matrix linking the points among themselves:

$$M_{b,ij} = \varphi\left(\left\|\vec{r}_{i,\text{in}} - \vec{r}_{j,\text{in}}\right\|/s_r\right) \quad (17)$$

After the resolution of the three systems of linear equations, the new coordinates of the points situated around the interface MNP/host matrix can be interpolated:

$$d_x(\vec{r}) = \sum_{j=1}^{n_b} \alpha_j^x \varphi\left(\left\|\vec{r} - \vec{r}_{j,\text{in}}\right\|\right) + \beta_1^x + \beta_2^x x + \beta_3^x y + \beta_4^x z \quad (18)$$

$$d_y(\vec{r}) = \sum_{j=1}^{n_b} \alpha_j^y \varphi\left(\left\|\vec{r} - \vec{r}_{j,\text{in}}\right\|\right) + \beta_1^y + \beta_2^y x + \beta_3^y y + \beta_4^y z \quad (19)$$

$$d_z(\vec{r}) = \sum_{j=1}^{n_b} \alpha_j^z \varphi\left(\left\|\vec{r} - \vec{r}_{j,\text{in}}\right\|\right) + \beta_1^z + \beta_2^z x + \beta_3^z y + \beta_4^z z \quad (20)$$

3 RESULTS

3.1 Description of the systems studied: nanoparticle shapes and vibration eigenmodes considered

We studied the acousto-plasmonic coupling mechanisms for three types of gold nanoparticles embedded in a homogeneous dielectric host matrix which refractive index is equal to 1.3 (**Fig. 3a**). The Lamé parameters describing gold elastic properties are taken from reference 51. **Figure 3b** shows the extinction cross sections of the nanoparticles in the absence of acousto-plasmonic coupling. The first nanoparticle is a sphere which radius is equal to 30 nm. It supports a localized plasmon mode at 527.5 nm. The second nanoparticle is a rod with a length of 61 nm and a width of 22 nm. The rod is built from a cylinder terminated by two hemispheres. The plasmonic resonance takes place at 669.6 nm in case of an incident electric field polarized along the length of the nanorod (**Fig. 3c**). The third nanoparticle is a triangular prism with a thickness of 25 nm. The geometrical parameters of the triangle are 50 nm for the height and for the base. The incident electric field is polarized along the triangle height (**Fig. 3c**) and the plasmonic resonance occurs at 601.6 nm.

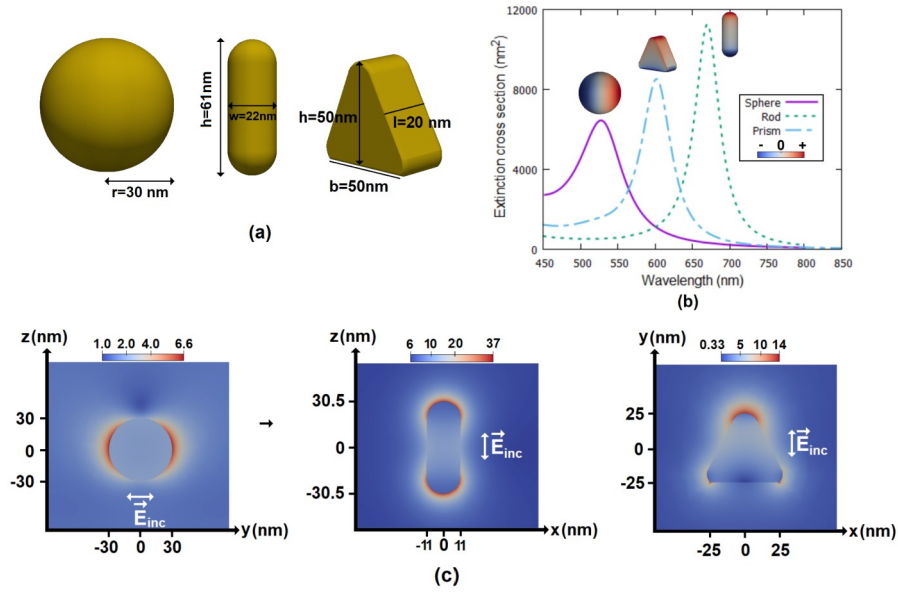


Figure 3: (a) Geometrical parameters of the metallic nanoparticles studied. (b) Extinction cross sections of the metallic nanoparticles studied in absence of acousto-plasmonic coupling and 3D surface charge distributions. (c) Electric field intensity around the MNPs at plasmon resonance.

The significance of the acousto-plasmonic coupling and the kind of mechanism involved depend on the acoustic mode considered. **Figure 4** represents the displacement field associated with the acoustic modes studied here. We considered five vibration modes including the fundamental radial mode of the sphere, also called breathing mode (**Fig. 4a**). The radial displacement field is alternatively positive and negative in the whole sphere. The contraction/dilatation movement involves volume variations but no changes of the shape. Unlike the breathing mode, confined quadrupolar vibrations of the sphere induces modifications of the aspect ratio (**Fig. 4b**). The radial field displacement presents two poles with an orientation towards the outside of the sphere, and two other poles with an orientation towards the inside of the sphere. This causes an extension of the sphere diameter along one axis and a contraction along a perpendicular axis. Concerning the extension/contraction mode of the rod length, we notice a slight variation of the width at the rod center, but the displacement principally takes place at the ends (**Fig. 4c**). For the breathing vibration mode of the rod, it is the contrary. The displacement field is more important at the center of the rod (**Fig. 4d**). Finally, the stretching/shrinking mode of the corners of the prism shows a more intense displacement field at the base corners because the prism cross section is an isosceles triangle (**Fig. 4e**). When the corners are stretched, the radial displacement field at the middle of the edges and the faces is oriented towards the inside of the prism and inversely.

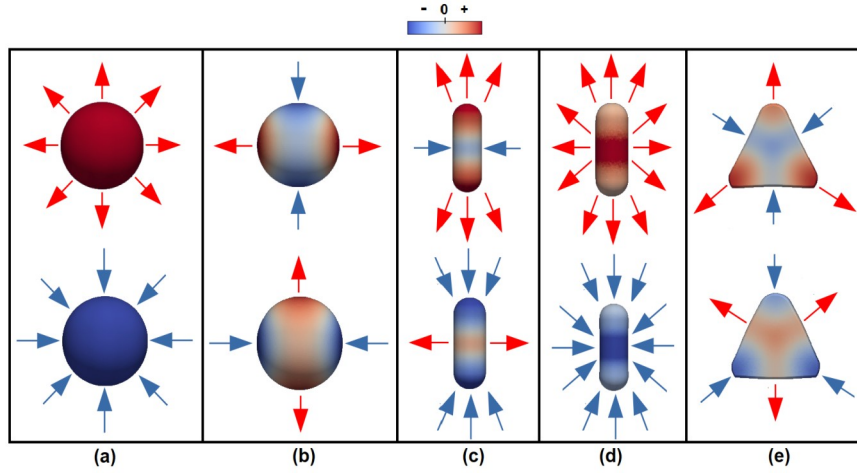


Figure 4: Radial displacement field of the vibration eigenmodes considered (The origin of the Cartesian coordinate system is situated at the nanoparticles center.). The MNP are represented in 3 dimensions. The color bar indicates the relative magnitude of the displacement. The arrows show the in-plane relative displacement direction. **(a)** Breathing mode of the sphere (50.6 GHz) **(b)** Quadrupolar spheroidal mode of the sphere (16.9 GHz) **(c)** Extension/contraction mode of the rod length (18.4 GHz) **(d)** Breathing mode of the rod (110.3 GHz) **(e)** Stretching/shrinking mode of the prism corners (23.0 GHz).

3.2 Nanosphere results

Figure 5 shows the effect of the three kind of phonon-plasmon coupling mechanisms on the position of the sphere plasmonic resonance. As a reminder, there is on one hand the optomechanical coupling (OM) which changes the nanoparticle shape (S). On the other hand, there is the photoelastic coupling (PE) with its two contributions: free electron density variation (ED) and deformation potential mechanism (DP). The vibrations associated with the fundamental breathing mode cause an increase and a decrease of the sphere radius (**Fig. 5a**). The LSPR position is linearly modulated by the radius variations. The LSPR wavelength increases when the radius increases and inversely for each coupling mechanisms involved. Consequently, the coupling mechanisms have cumulative contribution. Size variation effects on the LSPR position are very weak. Since this vibration mode doesn't change the spherical shape, volume coupling mechanisms are largely preponderant. We notice that the linear fit of the results obtained for the simulations taking into account all of the coupling mechanisms gives a slope more than three times superior to the one obtained from the simulations combining only shape and ED effects. So, DP mechanism is the main phonon-plasmon coupling mechanism for the fundamental breathing mode of the sphere. The fundamental quadrupolar vibration mode couples with the plasmonic mode in a drastically different

way (**Fig. 5b**). There is no volume coupling mechanisms involved and the LSPR position is only affected by shape effects. During vibrations, the sphere loses its spherical shape. The radius variation along (Ox) axis evolves in opposite phase with the ones along (Oy) and (Oz) axis. The MNP width becomes superior to its height when the sphere radius increases in (Ox) direction. As the incoming electric field is polarized along (Ox) axis, the LSPR wavelength increases.

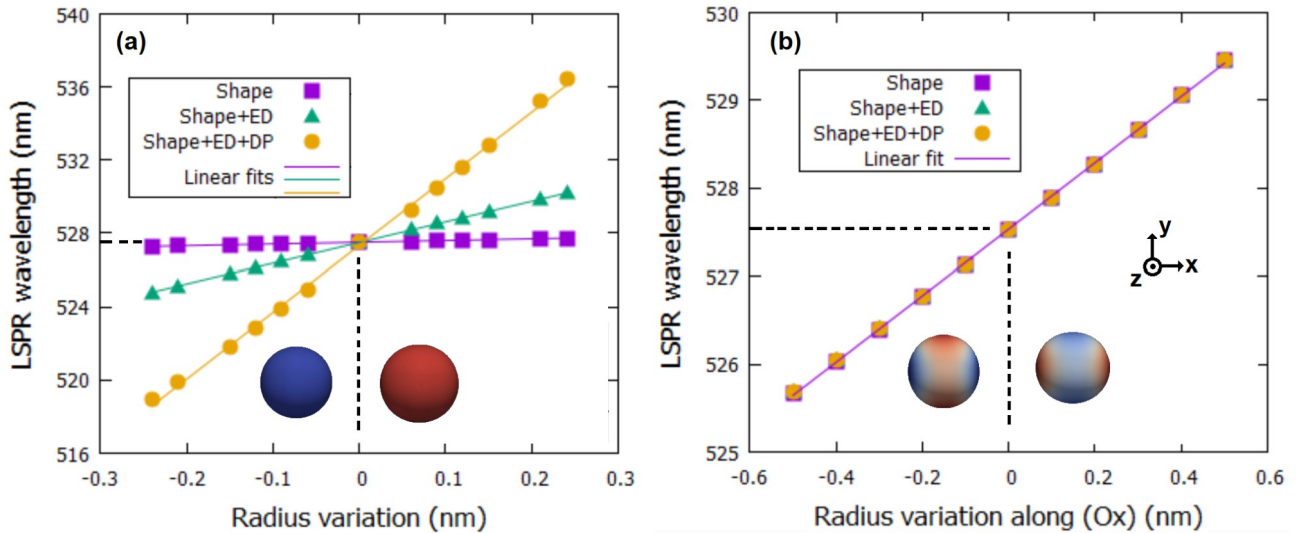


Figure 5: Influence of the acousto-plasmonic coupling mechanisms on the position of the sphere LSPR. For optical calculations, the incoming electric field is polarized along (Ox) axis. The black dashed lines highlights the undeformed MNP case. Concerning the MNP pictures inserted, the blue color corresponds to a negative radial field displacement and the red color to a positive one. **(a) Effect of the breathing mode (50.6 GHz).** The linear fits give slopes of 0.92 for the shape effect, 11.25 if shape and ED effects are taken into account and 36.43 if DP mechanism is added. **(b) Effect of the fundamental quadrupolar spheroidal vibration mode (16.9 GHz).** The linear fit gives a slope of 3.78 whatever the number of coupling mechanisms taken into account.

The two acoustic modes considered here doesn't have any impact on the LSPR peak width of the sphere (**Fig.6**). The breathing mode produces an increase of the peak amplitude when the sphere radius is reduced and inversely (**Fig. 6a**). This modulation is related to the DP mechanism. Indeed, **Fig. 6b** shows that the coupling based on shape and ED mechanisms slightly increases the peak amplitude when the sphere becomes bigger ($\Delta R=+0.2\text{nm}$). On the contrary, the DP mechanism contributes to decrease the peak amplitude. Concerning the effect of the fundamental quadrupolar vibration mode, it reduces the peak amplitude when the sphere radius along (Ox) axis decreases and inversely (**Fig. 6c**).

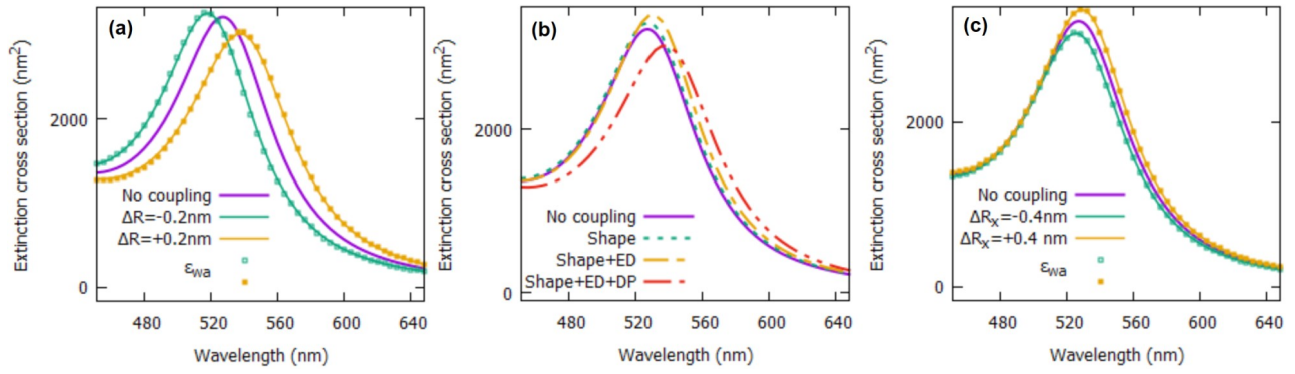


Figure 6: Influence of the acousto-plasmonic coupling on the LSPR extinction spectrum of the sphere. All the spectra are obtained using a local calculation of the relative permittivity except those pointed out by the symbol ϵ_{wa} (wa: weighted average). **(a)** Influence of the breathing mode (50.6 GHz). **(b)** Contribution of each coupling mechanism for the breathing mode in case of a radius variation equal to $\Delta R=+0.2\text{nm}$. **(c)** Influence of the fundamental quadrupolar vibration mode (16.9 GHz).

f_{vib}	$\Delta V/V$ (%)	Local relative permittivity			
50.6 GHz <i>Breathing mode</i>					-4.8 -2.6 $\text{Re}(\epsilon_r)$
					2.2 3.0 3.9 $\text{Im}(\epsilon_r)$
16.9 GHz <i>Quadrupolar mode</i>					-4.82 -4.75 -4.70 $\text{Re}(\epsilon_r)$
					2.34 2.36 2.39 $\text{Im}(\epsilon_r)$
	$\begin{matrix} z \\ \circ \rightarrow x \end{matrix}$	No elastic coupling	ED	ED+DP	

Figure 7: Local volume variations produced by the vibration modes of the sphere and their effect on the gold relative permittivity. The results depicted correspond to a radius variation equal to $\Delta R=+0.2\text{ nm}$ for the breathing mode and $\Delta R_x=-0.4\text{ nm}$ for the fundamental quadrupolar mode. The relative permittivity values are computed for the LSPR wavelength of the sphere without coupling ($\lambda=527.5\text{ nm}$). Data are drawn in the (x0z) plane.

Figure 7 illustrates the link between the trace of the strain tensor and the modulation of the relative permittivity of gold. The breathing mode creates volume variations taking the form of concentric spheres. The volume variations sign is the same all over the nanoparticle and their amplitude increases toward the sphere center. On the contrary, we notice that quadrupolar vibrations produce positive volume variations in one direction and negative ones in a perpendicular direction. Volume variations mainly occur at the nanoparticle surface and the trace of the strain tensor decreases in the sphere center direction. Surface acousto-plasmonic coupling mechanism doesn't change the gold relative permittivity. So, when we study the shape effect, the permittivity is still the same and constant all over the nanoparticle whatever the vibration mode considered. Colors

variations between the breathing and the quadrupolar mode in the column named "No elastic coupling" of **Fig. 7** are due to the use of different scales of colors in order to illustrate the effect of the free electron density variation and deformation potentials on the permittivity. We see that volume coupling mechanisms modulate the gold relative permittivity which becomes non-uniform.

The real part of the permittivity increases when the volume variation is positive and decreases when the volume variation is negative. Its value is -4.75 at λ_{LSPR} 527.5 nm in the absence of volume coupling mechanisms. If ED modulation is added, the real part of the permittivity varies between -4.71 and -4.11 for the breathing mode. The largest value is situated at the sphere center where the volume variation is also higher. For the quadrupolar mode, the real part varies between -4.77 and -4.73 . One of this value is slightly higher than the real part without coupling and corresponds to the poles where the volume variation is positive. The other value, slightly lower than the real part without coupling, corresponds to the poles where the volume variation is negative. This tendency grows when the DP mechanism is added and we notice that its influence is greater than the ED one.

Concerning the imaginary part of the permittivity, ED modulation and the DP mechanism have opposite effects. The imaginary part of the permittivity becomes lower when the volume variation is positive and inversely if the only one effect taken into account is ED. Thus, the imaginary part belongs to the interval $[2.22; 2.36]$ for the breathing mode and $[2.36; 2.37]$ for the quadrupolar mode, the value without coupling being 2.37. When DP mechanism is added, it counterbalances the ED effect. As a consequence, we notice an increase of the imaginary part when the volume variation is positive and inversely.

As the volume variations involved in the quadrupolar mode are less important than those involved in the breathing mode, we note a weaker modulation of the gold relative permittivity. Furthermore, the presence of poles with opposite signs suggests that by average effect over the whole nanoparticle, the modulation of the permittivity tends to be negligible. **Figure 6a** and **Fig. 6c** compare the extinction spectra obtained from a local evaluation of the gold relative permittivity and those obtained from a weighted average uniformly applied to the nanoparticle. The weighted average of the permittivity is calculated using the following formula:

$$\varepsilon_{r,wa}(\omega) = \frac{\sum_{i=1}^{nt} v_{f,i} \varepsilon_{r,i}(\vec{r}_{G,i}, \omega)}{V_f} \quad (21)$$

where nt is the number of tetrahedra constituting the nanoparticle mesh, $v_{f,i}$ and V_f are respectively the volume of the i^{th} tetrahedra and the total volume of the nanoparticle after the mechanical deformation, $\varepsilon_{r,i}$ is the local evaluation of the permittivity at the barycenter of the i^{th} tetrahedra under the influence of acoustic vibrations. **Figure 6** shows that the weighted average of gold permittivity

provides an accurate approximation of the optical response of the nanoparticle for both vibration modes. **Figure 8** shows that the average relative permittivity is not affected by the quadrupolar vibration mode. On the contrary, the average relative permittivity is affected by the breathing mode. The decrease of the free electron density when the sphere becomes bigger translates into an increase of the real part of the permittivity (**Fig. 8a**) and so, into a redshift of the LSPR wavelength. Concerning the imaginary part (**Fig. 8b**), it slightly decreases causing a soft increase of the LSPR peak amplitude (**Fig. 6b**, orange dashed curve). When DP mechanism is added, the real part of the permittivity increases more heavily (**Fig. 8a**) and the LSPR wavelength is redshifted. The imaginary part of the permittivity also heavily increases (**Fig. 8b**) bringing out the LSPR peak amplitude decrease observed for the red dashed curve on **Fig.6b**. On the other hand, as soon as the sphere contracts, the real part and the imaginary part of the permittivity decreases, the LSPR wavelength is blue-shifted and the peak amplitude increases (**Fig. 6a**, green curves).

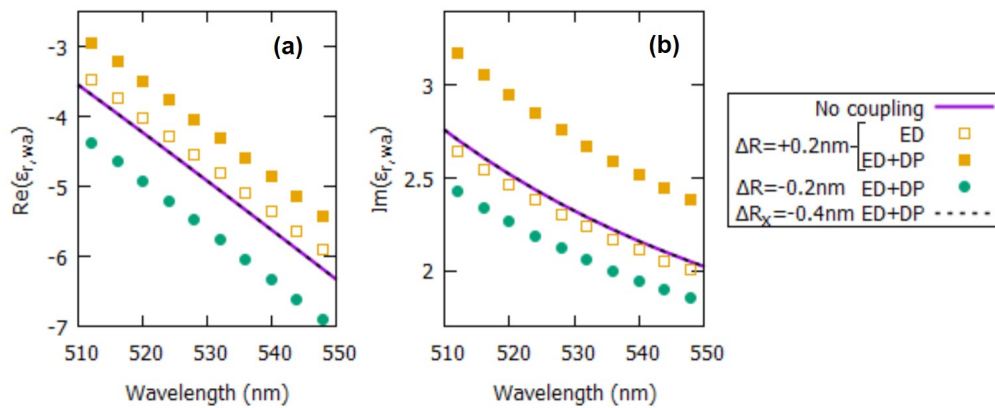


Figure 8: Weighted average of the local relative permittivity of gold for the breathing mode (orange squares and green circles) and for the fundamental quadrupolar mode (black dashed curves). The purple curves represent gold permittivity without coupling. **(a)** Real part of the permittivity. **(b)** Imaginary part of the permittivity.

3.3 Nanorod results

Figure 9 compares the linear modulation of the LSPR position under the influence of phonon-plasmon coupling for two different acoustic modes of the rod. The extension/contraction mode of the rod length is mainly affected by shape variations (**Fig. 9a**). The incoming electric field being polarized along (Oz) axis, the LSPR wavelength increases when the rod length increases and inversely. Contrary to the quadrupolar vibration mode of the sphere, this mode also slightly modulates the LSPR wavelength via ED variation and DP mechanisms. The slope is increased about 9.4% when ED variation mechanism is added to the shape effect. The additional slope increase when DP mechanism is taken into account is about 6.2%. **Figures 10 (a)** and **(b)** show the

variation of the gold permittivity produced by the photoelastic effect. When the rod length is stretched (orange squares), the real part of the permittivity increases for both kinds of photoelastic effects. Concerning the imaginary part, the variation of the free electron density causes a decrease whereas deformation potential mechanism causes an increase. However, the permittivity modulation is too weak to significantly affect the rod extinction cross section. So, the redshift of the LSPR position and the increase of the LSPR peak amplitude seen on **Fig. 11 (a)** are almost entirely due to optomechanical coupling.

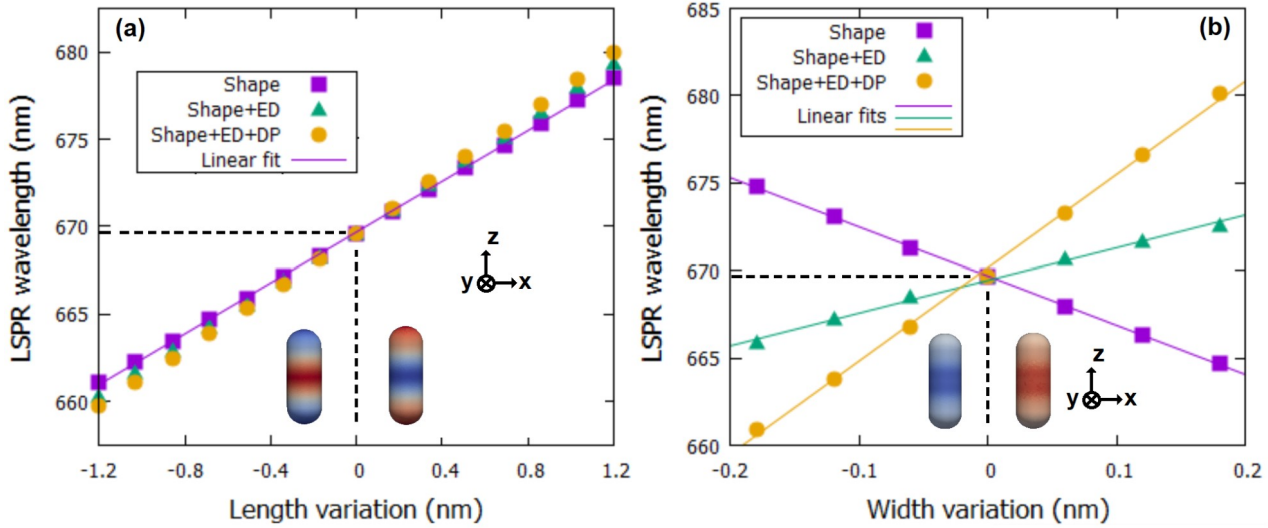


Figure 9: Influence of the acousto-plasmonic coupling mechanisms on the LSPR position of the rod. For optical calculations, the incoming electric field is polarized along (Oz) axis. The black dashed lines highlights the undeformed MNP case. Concerning the MNP pictures inserted, the blue color corresponds to a negative radial field displacement and the red color to a positive one. **(a) Effect of the extension/contraction mode of the rod length (18.4 GHz).** The linear fit give a slope of 7.26 for the shape effect. **(b) Effect of the breathing mode of the rod (110.3 GHz).** The linear fits give slopes of -28.08 for the shape effect, 18.65 if ED effect is added and 53.28 if all the coupling mechanisms are taken into account.

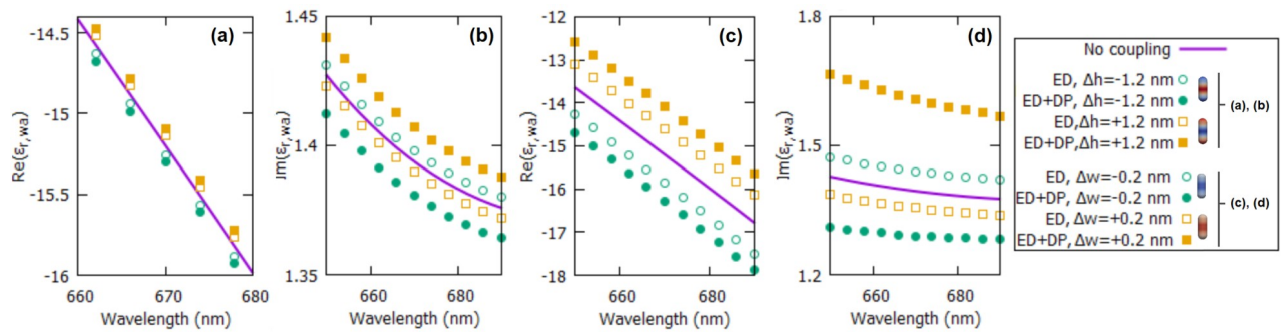


Figure 10: Weighted average of the local relative permittivity of gold. Real **(a)** and imaginary **(b)** part of the permittivity for the extension/contraction mode of the rod length. Real **(c)** and imaginary **(d)** part of the permittivity for the rod breathing mode. The solid purple curves represent gold permittivity without coupling.

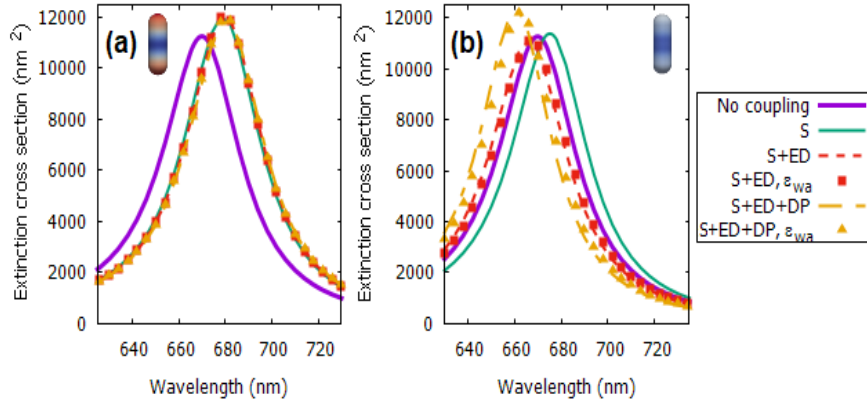


Figure 11: Influence of the acousto-plasmonic coupling on the LSPR extinction spectrum of the rod. All the spectra are obtained using a local calculation of the relative permittivity except those pointed out by the symbol ϵ_{wa} . The letter "S" refers to the shape effect. **(a)** Influence of the extension/contraction mode of the rod length (18.4 GHz) for a length variation equal to $\Delta h=+1.2$ nm. **(b)** Influence of the breathing mode (110.3 GHz) for a width variation equal to $\Delta w=-0.2$ nm.

The breathing mode of the rod reveals a different acousto-plasmonic coupling. **Fig. 9b** shows that the shape variation mechanism has opposite impact on the LSPR position compared to ED effect and DP mechanisms which have cumulative impact. Contrary to the breathing mode of the sphere, the breathing mode of the rod changes the MNP aspect ratio because it mainly affects the rod width. Consequently, the incoming field being polarized along (Oz) axis, the LSPR position increases when the rod width decreases and inversely. This mode is more heavily affected by PE coupling than the extension/contraction mode of the rod length. As for the sphere breathing mode, the modulation of the extinction spectra observed on **Fig. 11 (b)** can be related to the change of the average relative permittivity seen by the MNP under acoustic vibrations effect. There is a good agreement between the spectra calculated from a local evaluation of the gold relative permittivity over the MNP and those obtained using a weighted average. Concerning the OM coupling, it causes a redshift of the LSPR position due to the aspect ratio variation when the rod width is decreased (green curve). The peak amplitude is almost the same as the one without coupling because the imaginary part of the permittivity doesn't change a lot in that spectral range. The ED variation causes a decrease of the real part of the permittivity (**Fig. 10(c)**) and consequently a blue-shift of the LSPR position (red dashed curve). The increase of the imaginary part of the permittivity (**Fig. 10(d)**) slightly decreases the peak amplitude. DP mechanism decreases the real part and the imaginary part of the permittivity (**Figs. 10(c) and 10(d)**). As a consequence, the LSPR position is blue-shifted and the peak amplitude is increased (orange dashed curve).

Regarding the link between the trace of the strain tensor and the modulation of the relative permittivity of gold, we notice on **Fig. 12** that the tendency is the same as the one observed for the nanosphere vibrations studied. The more the volume variation is important, the more the

modulation of the permittivity is important. The real part increases when volume variation is positive and inversely. ED variation and DP mechanism have cumulative impact on the real part modulation. On the contrary, the ED variation leads to a decrease of the imaginary part when volume variation is positive and inversely. Furthermore, DP mechanism has an opposite impact which counterbalances the ED effect. As a consequence, when the two PE coupling mechanisms are taken into account, the imaginary part decreases if the volume variation is negative and increases if the volume variation is positive.

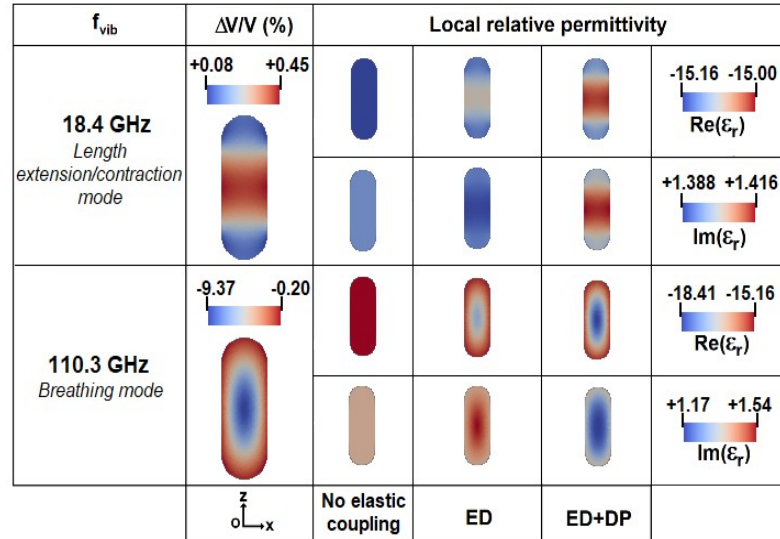


Figure 12: Local volume variations produced by the vibration modes of the rod and their effect on the gold relative permittivity. The results depicted correspond to a length variation equal to $\Delta h = +1.2$ nm for the length extension/contraction mode and a width variation equal to $\Delta w = -0.2$ nm for the breathing mode. The relative permittivity values are computed for the LSPR wavelength of the rod without coupling ($\lambda = 669.6$ nm). Data are drawn in the (xOz) plane.

3.4 Nanoprism results

Figure 13 (a) shows the linear modulation of the LSPR position by the stretching/shrinking mode of the prism corners. The resonance wavelength increases when the nanoprism height increases and inversely. The three kinds of acousto-plasmonic coupling mechanisms have cumulative impact on the LSPR position. We notice that the OM coupling is preponderant. Moreover, when the corners are stretched, the radial displacement field at the middle of the edges and faces is oriented towards the inside of the prism and inversely. The incoming electric field being polarized along the prism height, the LSPR modulation is in agreement with the aspect ratio change produced by acoustic vibrations. **Figure 13 (b)** points out the increase of the extinction cross

section at the plasmonic resonance when the MNP height is increased. The blue shift of the LSPR position when the MNP height is decreased goes with a decrease of the extinction cross section. We also see that calculations realized with the weighted average relative permittivity give a good approximation of the local calculations.

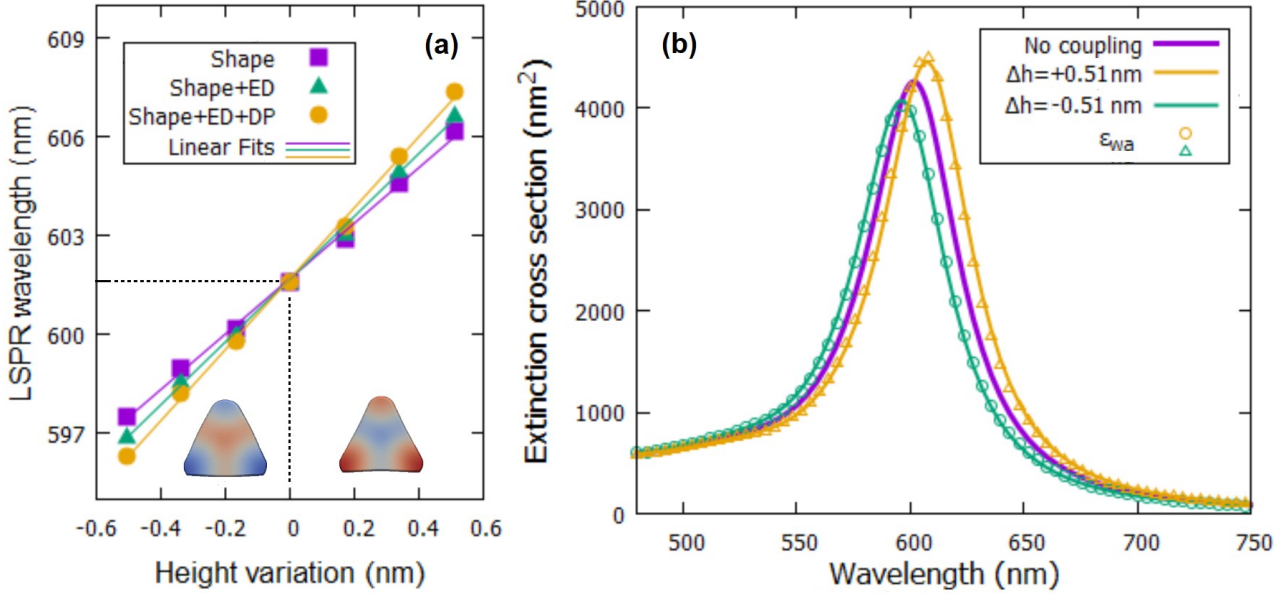


Figure 13: (a) Influence of the acousto-plasmonic coupling mechanisms on the LSPR position of the prism. The acoustic mode considered is the stretching/shrinking mode of the prism corners which occurs at 23.0 GHz. For optical calculations, the incoming electric field is polarized along (Oy) axis. The black dashed lines highlights the undeformed MNP case. Concerning the MNP pictures inserted, the blue color corresponds to a negative radial field displacement and the red color to a positive one. The linear fits give slopes of 8.40 for the shape effect, 9.52 if the shape and ED effects are taken into account and 10.76 if the DP mechanism is added. (b) Influence of the acousto-plasmonic coupling on the LSPR extinction spectrum of the prism (Shape+ED+DP). The spectra are obtained using a local calculation of the relative permittivity, except those pointed out by the symbol ϵ_{wa} , and for height variations equals to $\Delta h = \pm 0.51$ nm.

As the OM coupling mechanism is dominant, we expect a slight modulation of the gold relative permittivity by this particular acoustic vibration mode which is confirmed by **Fig. 14(a) and (b)**. The ED variation and the DP mechanism have cumulative effects on the real part of the permittivity. We observe an increase when the prism height is increased and a decrease when the prism height is decreased which is in accordance with the LSPR position variation. **Figure 14 (c)** shows that the height increase is associated with a positive volume variation which is more important at the prism center. On the contrary, the height decrease is associated with a negative volume variation. Concerning the imaginary part of the permittivity, ED variation and DP mechanism have opposite effects. In this way, when the prism height is decreased, and so when the volume variation is negative, the imaginary part increases. This is depicted on **Fig. 14(c)** by the color change from light grey to light red between "No elastic coupling" column and "ED" column (line 4). DP mechanism have an opposite and more important effect. Consequently, when it is added in calculations, the

imaginary part decreases and we see a color change from light red to blue between "ED" column and "DP" column. Finally, the local permittivity variations are more important in the regions where volume variations are more important for both real and imaginary part.

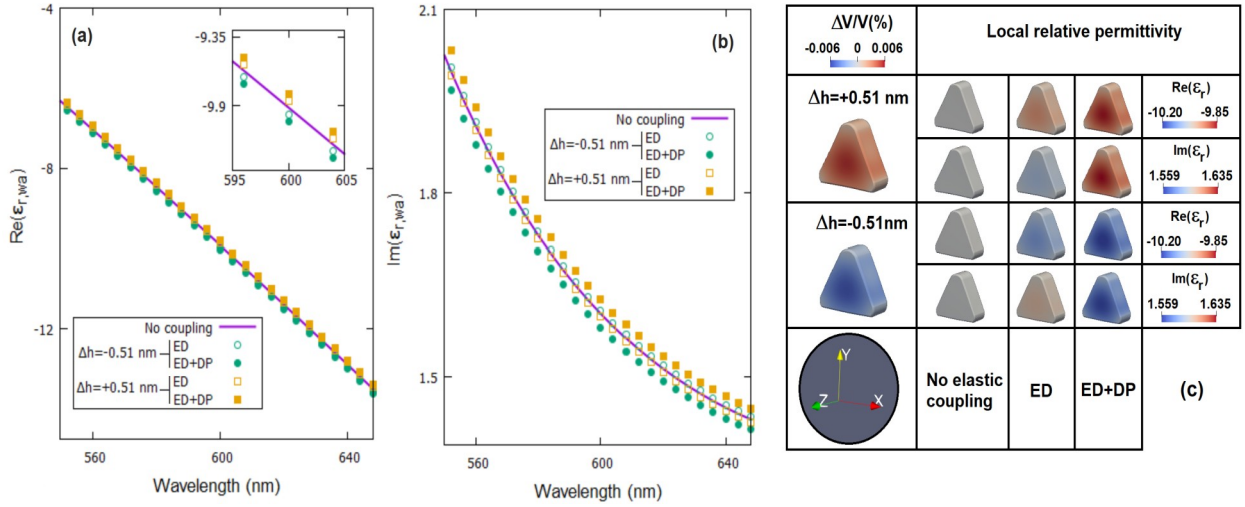


Figure 14: Weighted average of the local relative permittivity of gold. Real (a) and imaginary (b) part for the stretching/shrinking mode of the prism corners (23.0 GHz). The purple curves represent gold permittivity without coupling. (c) Local volume variations produced by the vibration mode of prism and their effect on the gold relative permittivity. The relative permittivity values are computed for the LSPR wavelength of the prism without coupling ($\lambda=601.6$ nm).

5. CONCLUSION

We have developed a computational method that allows to explore how acoustic vibrations modulate the optical response of metallic nanoparticles. Our approach is based on the use of open-source softwares including the finite element software FreeFEM. Our numerical method determines one after the other the acoustic modes of the nanoparticles, the local changes induced by the PE coupling on the metal dielectric permittivity derived from a previous model²⁷ and the modulation of the optical response produced by both PE and OM coupling. Calculations, realized for different deformation amplitudes, allow to determine the linear modulation of the LSPR position and to separately evaluate the contribution of each kind of coupling mechanism. As OM coupling changes the MNP shape and so its aspect ratio, its effect on the optical response is related to the polarization of the incoming electric field. It emerges from our theoretical results that PE coupling is more significant in the nanoparticle regions where local volume variations are more important. It increases both the real and the imaginary part of the permittivity when volume variation is positive and inversely. The two kinds of PE coupling mechanisms have an opposite impact on the imaginary part modulation. Indeed, the ED variation induces a decrease of the imaginary part when volume

variation is positive and inversely. The effect of DP mechanism is more important and counterbalances the free electron density variation effect. Local variations of the dielectric permittivity have an average impact on the nanoparticle optical response. Thus, it is possible to calculate a weighted average permittivity which is the same all over the nanoparticle. It allows to predict how an acoustic vibration eigenmode will modulate the nanoparticle optical response. Indeed, if acoustic strains cause an increase of the real and imaginary part of the permittivity, the plasmonic response will be redshifted and the peak amplitude decreased. The work presented here gives insights which may be useful to interpret pump-probe experiments results and guidelines to select the MNP geometry or the probe laser wavelength⁵². It also provides a foundation for the study of the acousto-plasmonic coupling in case of MNP composed of another metals than gold or in more complex nano-systems. Obviously, handling external mechanical interaction is important in order to be able to describe realistic systems. If this work is essentially methodological, even if it gives as well several physical insights in acousto-plasmonic coupling, our method could be extended to describe the mechanical interaction of a metal nanosystem with a material environment. The principle is, similarly to pure optical or elastic FEM simulations, to use perfectly matched layers to prevent reflection at the computational domain boundaries of elastic and electromagnetic waves scattered from nanoparticles. If the environment consists of dielectric materials, the photo-elastic interaction can be described using tabulated photoelastic constant.⁵³ Knowing that localized surface plasmon are mostly sensitive to modifications of the environment within the near-field zone (of sub-wavelength extension around the nanoparticle), it is expected that the strength of the interaction will rapidly stabilize when increasing the size of the simulation domain. Finally, our method to transfer the deformed geometries between acoustic and optical calculations based on radial basis function interpolation is not limited to small deformations. As a consequence, it enables the investigation of acousto-optics interactions in nano-systems where large deformations can occur, for example in extended objects like nanowires and micro-pillars, or in case of flexible substrates such as PDMS substrates which can be applied in strain sensing⁵⁴.

SUPPORTING INFORMATION

Validation results of the numerical method

REFERENCES

- 1 Prieto, G.; Zečević, J.; Friedrich, H.; de Jong, K. P.; de Jongh, P. E. Towards Stable Catalysts by Controlling Collective Properties of Supported Metal Nanoparticles. *Nat. Mater.* **2013**, *12*, 34-39.
- 2 Hassan, S.; Prakash, G.; Ozturk, A.; Saghadzadeh, S.; Sohail, M. F.; Seo, J.; Dockmeci, M.; Zhang, Y. S.; Khademhosseini, A. Evolution and Clinical Translation of Drug Delivery Nanomaterials. *Nano Today* **2017**, *15*, 91-106.
- 3 Choi, S.; Johnson, B. C.; Castelletto, S.; Ton-That, C.; Phillips, M. R.; Aharonovich, I. Single Photon Emission from ZnO Nanoparticles. *Appl. Phys. Lett.* **2014**, *104*, 261101.
- 4 Pakizeh, T.; Käll, M. Unidirectional Ultracompact Optical Nanoantennas. *Nano Lett.* **2009**, *9*, 2343-2349.
- 5 Li, B.; Zu, S.; Zhou, J.; Jiang, Q.; Du, B.; Shan, H.; Luo, Y.; Liu, Z.; Zhu, X.; Fang, Z. Single-Nanoparticle Plasmonic Electro-Optic Modulator Based on MoS₂ Monolayers. *ACS Nano* **2017**, *11*, 9720-9727.
- 6 Unser, S.; Bruzas, I.; He, J.; Sagle, L. Localized Surface Plasmon Resonance Biosensing: Current Challenges and Approaches. *Sensors* **2015**, *15*, 15684-15716.
- 7 Ahijado-Guzmán, R.; Prasad, J.; Rosman, C.; Henkel, A.; Tome, L.; Schneider, D.; Rivas, G.; Sönnichsen, C. Plasmonic Nanosensors for Simultaneous Quantification of Multiple Protein-Protein Binding Affinities. *Nano Lett.* **2014**, *14*, 5528-5532.
- 8 Saison-Francioso, O.; Lévêque, G.; Boukherroub, R.; Szunerits, S.; Akjouj, A. Dependence between the Refractive-Index Sensitivity of Metallic Nanoparticles and the Spectral Position of their Localized Surface Plasmon Band: a Numerical and Analytical Study. *J. Phys. Chem. C* **2015**, *119*, 28551-28559.
- 9 Saison-Francioso, O.; Lévêque, G.; Akjouj, A.; Pennec, Y.; Djafari-Rouhani, B.; Szunerits, S.; Boukherroub, R. Plasmonic Nanoparticles Array for High-Sensitivity Sensing: a Theoretical Investigation. *J. Phys. Chem. C* **2012**, *116*, 17819-17827.
- 10 Adichtchev, S.; Sirotkin, S.; Bachelier, G.; Saviot, L.; Etienne, S.; Stephanidis, B.; Duval, E.; Mermet, A. Higher-Order Vibration Modes of Bimetallic Ag-Au Nanoparticles Embedded in Glass. *Phys. Rev. B* **2009**, *79*, 201402.
- 11 Tripathy, S.; Marty, R.; Lin, V. K.; Teo, S. L.; Ye, E.; Arbouet, A.; Saviot, L.; Girard, C.; Han, M. Y.; Mlayah, A. Acousto-Plasmonic and Surface-Enhanced Raman Scattering Properties of Coupled Gold Nanospheres/Nanodisk Trimers. *Nano Lett.* **2011**, *11*, 431-437.
- 12 Crut, A.; Maioli, P.; Del Fatti, N.; Vallée, F. Acoustic Vibrations of Metal Nano-Objects : Time-Domain Investigations. *Phys. Rep.* **2015**, *549*, 1-43.
- 13 Dacosta Fernandes, B.; Spuch-Calvar, M.; Baida, H.; Tréguer-Delapierre, M.; Oberlé, J.; Langot, P.; Burgin, J. Acoustic Vibrations of Au Nano-Bipyramids and their Modification under Ag Deposition: a Perspective for the Development of Nanobalances. *ACS Nano* **2013**, *7*, 7630-7639.
- 14 Voisin, C.; Del Fatti, N.; Christofilos, D.; Vallée, F. Ultrafast Electron Dynamics and Optical Nonlinearities in Metal Nanoparticles. *J. Phys. Chem. B* **2001**, *105*, 2264-2280.
- 15 Bonacina, L.; Callegari, A.; Bonati, C.; van Mourik, F.; Chergui, M. Time-Resolved Photodynamics of Triangular-Shaped Silver Nanoplates. *Nano Lett.* **2006**, *6*, 7-10.
- 16 Margueritat, J.; Gonzalo, J.; Afonso, C.; Mlayah, A.; Murray, D. B.; Saviot, L. Surface Plasmons and Vibrations of Self-Assembled Silver Nanocolumns. *Nano Lett.* **2006**, *6*, 2037-2042.
- 17 Larsson, E. M.; Alegret, J.; Käll, M.; Sutherland, D. S. Sensing Characteristics of NIR Localized Surface Plasmon Resonances in Gold Nanorings for Application as Ultrasensitive Biosensors. *Nano Lett.* **2007**, *7*, 1256-1263.
- 18 Chen, H.; Kou, X.; Yang, Z.; Ni, W.; Wang, J. Shape- and Size-Dependent Refractive Index Sensitivity of Gold Nanoparticles. *Langmuir* **2008**, *24*, 5233-5237.
- 19 Bukasov, R.; Shumaker-Parry, J. S. Highly Tunable Infrared Extinction Properties of Gold Nanocrescents. *Nano Lett.* **2007**, *7*, 1113-1118.
- 20 Oumekloul, Z.; Moutaouekkil, M.; Lévêque, G.; Talbi, A.; Mir, A.; Akjouj, A. Nanomechanical

- Modulation Cavities of Localized Surface Plasmon Resonance with Elastic Whispering-Gallery Modes. *J. Appl. Phys.* **2020**, *127*, 023105.
- 21 El-Jallal, S.; Mrabti, A.; Lévêque, G.; Akjouj, A.; Pennec, Y.; Djafari-Rouhani, B. Phonon Interaction with Coupled Photonic-Plasmonic Modes in a Phoxonic Cavity. *AIP Adv.* **2016**, *6*, 122001.
 - 22 Mrabti, A.; Lévêque, G.; Akjouj, A.; Pennec, Y.; Djafari-Rouhani, B.; Nicolas, R.; Maurer, T.; Adam, P.-M. Elastoplasmonic Interaction in Metal-Insulator-Metal Localized Surface Plasmon Systems. *Phys. Rev. B* **2016**, *94*, 075405.
 - 23 Gomis-Bresco, J.; Navarro-Urrios, D.; Oudich, M.; El-Jallal, S.; Griol, A.; Puerto, D.; Chavez, E.; Pennec, Y.; Djafari-Rouhani, B.; Alzina, F. et al. One-Dimensional Optomechanical Crystal with a Complete Phononic Band Gap. *Nat. Commun.* **2014**, *5*, 4452.
 - 24 Song, C.; Li, F.; Guo, X.; Chen, W.; Dong, C.; Zhang, J.; Zhang, J.; Wang, L. Gold Nanostars for Cancer Cells-Targeted SERS-Imaging and NIR Light-Triggered Plasmonic Photothermal Therapy (PPTT) in the First and Second Biological Windows. *J. Mater. Chem. B* **2019**, *7*, 2001-2008.
 - 25 O' Brien, K.; Lanzillotti-kimura, N. D.; Rho, J.; Suchowski, H.; Yin, X.; Zhang, X. Ultrafast Acousto-Plasmonic Control and Sensing in Complex Nanostructures. *Nat. Commun.* **2014**, *5*, 4042.
 - 26 Deacon, W. M.; Lombardi, A.; Benz, F.; del Valle-Inclan Redondo, Y.; Chikkaraddy, R.; de Nijs, B.; Kleemann, M.-E.; Mertens, J.; Baumberg, J. J. Interrogating Nanojunctions Using Ultraconfined Acoustoplasmonic Coupling. *Phys. Rev. Lett.* **2017**, *119*, 023901.
 - 27 Ahmed, A.; Pelton, M.; Guest, J. R. Understanding How Acoustic Vibrations Modulate the Optical Response of Plasmonic Metal Nanoparticles. *ACS Nano* **2017**, *11*, 9360-9369.
 - 28 Bachelier, G.; Mlayah, A. Surface Plasmon Mediated Raman Scattering in Metal Nanoparticles. *Phys. Rev. B* **2004**, *69*, 205408.
 - 29 Bardeen, J.; Shockley, W. Deformation Potentials and Mobilities in Non-Polar Crystals. *Phys. Rev.* **1950**, *80*, 72-80.
 - 30 de Boer, A.; van der Schoot, M. S.; Bijl, H. Mesh Deformation Based on Radial Basis Function Interpolation. *Comput. Struct.* **2007**, *85*, 784-795.
 - 31 Marty, R.; Arbouet, A.; Girard, C.; Mlayah, A.; Paillard, V.; Lin, V. K.; Teo, S. L.; Tripathy, S. Damping of the Acoustic Vibrations of Individual Gold Nanoparticles. *Nano Lett.* **2011**, *11*, 3301-3306.
 - 32 *Theory of Elasticity*; Landau, L. D., Lifshitz, E. M., Eds.; Pergamon Press: Oxford, 1975.
 - 33 *Introduction to Linear Elasticity*; Gould, P. L., Eds.; Springer: New York, 2013.
 - 34 Juvé, V.; Crut, A.; Maioli, P.; Pellarin, M.; Broyer, M.; Del Fatti, N.; Vallée, F. Probing Elasticity at the Nanoscale: Terahertz Acoustic Vibration of Small Metal Nanoparticles. *Nano Lett.* **2010**, *10*, 1853-1858.
 - 35 Stoll, T.; Maioli, P.; Crut, A.; Burgin, J.; Langot, P.; Pellarin, M.; Sánchez-Iglesias, A.; Rodríguez-González, B.; Liz-Marzán, L. M.; Del Fatti, N. et al. Ultrafast Acoustic Vibrations of Bimetallic Nanoparticles. *J. Phys. Chem. C* **2015**, *119*, 1591-1599.
 - 36 Kahnert, F. M. Numerical Methods in Electromagnetic Scattering Theory. *J. Quant. Spectrosc. Radiat. Transfer* **2003**, *79-80*, 775-824.
 - 37 Szczepanek, P.; Glosser, R. Piezo-Optical Constants of Gold. *Solid State Commun.* **1974**, *15*, 1425-1429.
 - 38 *Fundamentals of Finite Element Analysis: Linear Finite Element Analysis*; Koutromanos, I., McClure, J., Roy, C., Eds.; John Wiley & Sons: Hoboken, 2018.
 - 39 *Theory and Computation of Electromagnetic fields*; Jin, J.-M., Eds.; John Wiley & Sons: Hoboken, 2010.
 - 40 *Finite Element Method*; Dhatt, G., Touzot, G., Lefrançois, E., Eds.; John Wiley & Sons: Hoboken, 2012.
 - 41 Sadiku, M. N. O. A Simple Introduction to Finite Element Analysis of Electromagnetic Problems. *IEEE Trans. Educ.* **1989**, *32*, 85-93.

- 42 Gould, N. I. M.; Scott, J. A.; Hu, Y. A Numerical Evaluation of Sparse Direct Solvers for the Solution of Large Sparse Symmetric Linear Systems of Equations. *ACM Trans. Math. Softw.* **2007**, *33*, 2, Article No.10.
- 43 Geuzaine, C.; Remacle, J.-F. Gmsh: A 3-D Finite Element Mesh Generator with Built-In Pre- and Post-Processing Facilities. *Int. J. Numer. Meth. Eng.* **2009**, *79*, 1309-1331.
- 44 Hecht, F. New Development in FreeFem++. *J. Numer. Math.* **2012**, *20*, 251-266.
- 45 Nédélec, J. C. Mixed Finite Elements in R^3 . *Num. Math.* **1980**, *35*, 315-341.
- 46 VTK: Process Images and Create 3D Computer Graphics with the Visualization Toolkit. <https://vtk.org/> (accessed January 16, 2020).
- 47 ParaView: an open-source, multi-platform data analysis and visualization application. <https://www.paraview.org/> (accessed January 16, 2020).
- 48 Biancolini, M. E.; Chiappa, A.; Giorgetti, F.; Porziani, S.; Rochette, M. Radial Basis Functions Mesh Morphing for the Analysis of Cracks Propagation. *Procedia Struct. Integrity* **2018**, *8*, 433-443.
- 49 Bos, F. M.; van Oudheusden, B. W.; Bijl, H. Radial Basis Function Based Mesh Deformation Applied to Simulation of Flow Around Flapping Wings. *Comput. Fluids* **2013**, *79*, 167-177.
- 50 Niu, J.; Lei J.; He J. Radial Basis Function Mesh Deformation Based on Dynamic Control Points. *Aerosp. Sci. Technol.* **2017**, *64*, 122-132.
- 51 Prost, A.; Poisson, F.; Bossy, E. Photoacoustic Generation by a Gold Nanosphere: From Linear to Nonlinear Thermoelastics in the Long-Pulse Illumination Regime. *Phys. Rev. B* **2015**, *92*, 115450.
- 52 Fuentes-Domínguez, R.; Smith, R. J.; Pérez-Cota, F.; Marques, L.; Peña-Rodríguez, O.; Clark, M. Size Characterisation Method and Detection Enhancement of Plasmonic Nanoparticles in a Pump-Probe System. *Appl. Sci.* **2017**, *7*, 819.
- 53 *Elastic Waves in Solids 1: Free and Guided Propagation*; Royer, D., Dieulesaint, E., Eds.; Springer-Verlag Berlin Heidelberg: Berlin, 2000.
- 54 Marae-Djouda, J.; Gontier, A.; Caputo, R.; Lévêque, G.; Bercu, B.; Madi, Y.; Montay, G.; Adam, P.-M.; Molinari, M.; Stagon, S.; Maurer, T. Dense Brushes of Tilted Metallic Nanorods Grown onto Stretchable Substrates for Optical Strain Sensing. *ACS Appl. Nano Mater.* **2018**, *1*, 2347–2355.